BULLETIN OF THE POLISH ACADEMY OF SCIENCES
TECHNICAL SCIENCES, Vol. 70(4), 2022, Article number: e141721
DOI: 10.24425/bpasts.2022.141721

Modeling and energy recovery from a system with two pseudo-levitating magnets

Andrzej MITURA* and **Krzysztof KECIK**

Faculty of Mechanical Engineering, Department of Applied Mechanics, Lublin University of Technology, Nadbystrzycka 36, 20-618 Lublin, Poland

Abstract. In this paper, a model of an electromagnetic system with two levitating magnets is presented. Modeling was performed using the results of experiments. The data obtained make it possible to fit the magnetic forces between two magnets using a 5^{th} order polynomial. The time series show that dry friction constitutes an important part of damping forces. The differential equations of motion consider strong nonlinearities of magnetic and damping forces. These terms cause the nonlinear hardening effect. The energy recovered by magnetic induction is dissipated in the resistors. Numerical simulations show that resistance has an impact on magnet dynamics and energy recovery. From the resonance characteristics obtained, optimal resistance is determined when energy recovery is the highest.

Key words: energy recovery, pseudo-levitating magnets, nonlinear dynamics, experimental research.

1. INTRODUCTION

Climate changes require a new perspective on energy issues. Global air pollution and the greenhouse effect make it necessary to find alternative sources of energy. For example, the European Union is implementing an energy transformation program. The foreseen changes are described in [1]. Some aspects of the so-called green energy transformation in Poland are described in [2]. Among others, the research object (Arena Przywidz building) and proposed modifications in its thermal and electrical installation are described. The author shows the contribution of the Institute of Fluid-Flow Machinery of the Polish Academy of Sciences to the Polish green energy transformation. However, the best solution would be to reduce energy demand altogether. Therefore, in the literature, one can find many studies on energy recovery. The inclusion of such devices in the energy mix could be advantageous because their production is related to existing processes. For example, walking, sport and dancing are associated with human activities. The feet generate pressure forces on the ground. This effect can be used for energy recovery, especially in public places. In [3], the application of a mat prototype with piezoelectric elements is considered. This mat can be located on the floor, for example in a supermarket, and it will allow energy harvesting from human feet steps. The authors present the results of their research, concluding that energy of 0.0604 W can be recovered from ten human steps. It can be used to supply devices with low energy consumption. The results of similar studies are presented in [4]. Pasquale *et al.* compared two strategies with piezoelectric or electromagnetic transducers. The proposed harvesters were embedded in clothes, and energy was recovered from human body motion. The study indicated higher efficiency of the electromagnetic device. It can recover power of 0.7 mW, while the piezoelectric element can generate about 0.33 μW. The machines running continuously are better objects for energy harvesting. During normal operation, they usually generate vibrations. Implementing an additional harvester subsystem on the machine can convert some mechanical energy into electricity. In this case, the literature also mentions mainly piezoelectric or electromagnetic harvesters. Applications for these devices are the most widely proposed. Review studies [5, 6] discuss various aspects of piezoelectric solutions, providing data about the sources of information about different ways of modeling piezoelectric elements, popular electrical circuits used for energy recovery, and selected applications. Sarker *et al.* published a similar review article, but for electromagnetic harvesters [7]. The goal of the paper was to organize the state of the art and suggest a low power smart sensor circuit that would harvest energy from an electromagnetic solution. An analysis of the data in [5–7] demonstrates that both devices use different effects to convert energy. These are magnetic induction and piezoelectric effect for electromagnetic and piezoelectric harvesters, respectively. A very sound comparison of selected devices from both groups is presented in [8]. Bo and Gardonio analyzed two appropriately chosen seismic vibration energy harvesters. It is important that the authors tried to obtain solutions with identical properties wherever it was possible. For example, the proposed harvester subsystems had the same mass and natural frequencies. The results showed that for the implementation of optimal real impedance, the maximum recovery power was 0.04 W and 0.02 W for the electromagnetic and piezoelectric transducers, respectively. Under comparable conditions, the effectiveness of both solutions was similar. Thus, the choice of a harvester type may depend on individual characteristics of the base object. The studies presented above are characterized by low energy recovery efficiency. In the literature, some suggestions on how

*e-mail: a.mitura@pollub.pl

Manuscript submitted 2021-11-14, revised 2022-05-07, initially accepted for publication 2022-05-24, published in August 2022.

to increase energy power obtained are given. Ostrowski *et al.* present the concept of a mechanical amplifier inserted between a mechanical object and an electromagnetic harvester [9]. Mechanical vibrations, i.e. relative displacement between sprung and unsprung masses in a car suspension, were strengthened by the amplifier using a gear. This mechanical amplifier can multiply kinematic excitation of the electromagnetic harvester. In most studies, the harvester electrical circuit consists of a resistor. This is the easiest way to recover energy. However, it might not be useful in that many applications. An alternative to this solution is the idea presented in [10]. The authors proposed using an electromagnetic subsystem as a generator. Obtained electricity could thus be used for self-powering a magnetorheological damper. This solution is interesting because the vibration control adaptation is performed automatically. The electromagnetic subsystem can replace the controller, i.e. it performs the measurement function and acts as the external power source.

The first joint research of the authors of this paper was an analysis of non-linear vibration absorption using a pendulum [11]. The pendulum swing eliminated vibration of the research object (single oscillator). In subsequent studies, attempts were made to recover energy from the pendulum's movement. The pendulum is not very deformable, so electromagnetic devices were predisposed in this case. In [12], two independent concepts of electromagnetic harvesters were considered. The first harvester was a rotary device, with its axis of rotation interconnected with that of the pendulum. The second solution was a subsystem with one levitating magnet (so-called maglev system) mounted inside the pendulum. The energy recovery effectiveness of both variants was tested independently. The rotary harvester could limit the pendulum swing and reduce vibration absorption of the base object. The maglev harvester proved a better solution because the generated modification of the pendulum dynamics was lower. In other studies [13, 14], the pendulum with a built-in maglev subsystem was excited kinematically. It was fixed on the shaker armature instead of the base object. Experimental and numerical studies showed a nonlinear trend of the electromechanical coupling coefficient [13] and existence of the so-called electrical suppression [14]. Similar conclusions were also drawn by other researchers. Sneller and Mann presented theoretical relationships between induced voltage, magnet relative velocity and nonlinear electromechanical coupling [15]. The function of nonlinear coupling was compared to the coil flux linkage, and it depended on the magnet position in relation to the inductive coil. The curve of electromechanical coupling was described using Taylor series expansion. In [9], the nonlinear trend of electromechanical coupling was described using the Fourier series approximation. A polynomial function was applied to estimate electromechanical coupling in [13]. This problem is often simplified to a constant coefficient of electromechanical coupling. In [16], an equivalent constant coefficient was estimated by four different methods. These methods included experimental testing and finite element analysis. Obtained values were similar, with the maximum deviation of about 5%. It is important to stress that the value was obtained for small vibrations. The possibility of increasing the energy recovery level from the classical maglev system with one movable magnet seems to be limited. Therefore, new modifications of this harvester structure are designed. The easiest solution is to add a second movable magnet. Abed *et al.* proposed a 2 DOF model of the maglev system [17]. In the description of the forces between the magnets, nonlinear terms were included. The quadratic and cubic terms of magnetic forces were used in the equation of motion. However, linear damping was assumed. The authors determined the system dynamics and energy recovery. For example, a hardening effect was detected. In this model, dry friction was not included. It can be caused by some imperfections, for example a gap between a movable magnet and a tube. Green *et al.* tested the possibility of using three models: Coulomb, hyperbolic tangent and LuGre to describe friction [18]. It was assumed that normal force at contact was constant. This simplifies the friction problem to a significant extent. Generally, in many studies, the friction effect is neglected [17] or inadequately considered [18]. However, the authors' own observations indicate that this assumption is not correct. For low levels of excitations, a problem with starting magnet vibration is often visible during tests. This problem was an inspiration for research on friction in a levitation system. However, this issue is not well described in the literature. In the latest research, Kecik and Mitura showed that friction was variable in a system with one levitating magnet [19]. The designated mathematical model and experimental tests allowed establishment of a relationship between frictional and repel forces. It was found that by reducing the distance between the magnets, normal and friction forces could be increased. This change could be described by means of a linear function. Generally, the effect of variable friction is not strong. However, the authors studied a system with one levitating magnet and a significant distance between the fixed magnets. This approach may be interesting in a system with two levitating systems. The addition of a movable magnet can radically change the level of friction forces.

This paper is a continuation of previous research. A significant modification in the previous prototype of the energy harvester is made by adding a second levitating magnet. The obtained system with two degrees of freedom has new properties, and they are investigated experimentally and numerically. In Section 2 "Model of a 2 DOF system", a strongly nonlinear mathematical model is proposed. Its parameters are determined via experimental testing. The effect of friction on the system dynamics is considered. In a subsequent section, the developed model is extended to include electrical elements (coils, resistors). Based on numerical simulations, the influence of the so-called electric damping on the dynamics and energy recovery is determined. Finally, a summary and conclusions are presented.

2. MODEL OF A 2 DOF SYSTEM

A schematic of the prototype device is shown in Fig. 1. The considered system was modeled as a 2 DOF system. The parameters were selected based on results from experimental tests. The schematic shows the most important elements of the system. Inside the plexiglass tube, there are two smaller fixed magnets B_1, B_2 and two larger movable magnets A_1, A_2. All mag-

nets are made of neodymium. The larger cylindrical magnets have a length of 35 mm and a diameter of 20 mm. The smaller magnets are rings with an outside diameter of 20 mm, an inside diameter of 5 mm, and a length of 5 mm. The hole diameter in the tube is 22 mm. The results show the presence of a gap between the tube and the magnets. Magnetic interactions cause levitation of the movable magnets. It is called pseudo-levitation because without a tube this effect would be impossible. The magnets induce repulsion, and they also try to turn around. Finally, two-point contact between the movable magnet and the tube is observed. This fact is also presented in Fig. 1. Motion of the elements is described relative to the stationary coordinate global system Ozx. The location of this coordinate system is related to the position of the center of B_1 when the system was not excited. Differential equations of motion with kinematic excitation can be written in a general form:

$$m_1\ddot{z}_1 - F_{B1-A1} - F_{B2-A1} + F_{A2-A1} + F_{d1} + m_1 g + \alpha_1 i_1 = 0, \quad (1)$$

$$m_2\ddot{z}_2 + F_{B1-A2} + F_{B2-A2} - F_{A2-A1} + F_{d2} + m_2 g + \alpha_2 i_2 = 0, \quad (2)$$

where z_1, z_2 are the coordinates of the absolute magnet movements, and $m_1 = m_2 = 0.09$ kg are the movable magnet masses.

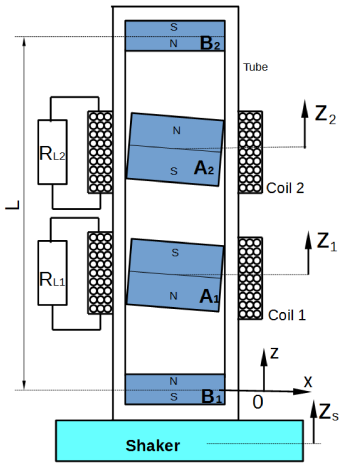

Fig. 1. Schematic of an electromagnetic system

Forces F with an appropriate subscript are the magnetic (indexes using magnet symbols) or damping forces (indexes using the letter d) identified via experimental testing. The tube is mounted onto the shaker armature, the motion of which is described by z_s. This kinematic excitation is hidden in the magnetic forces, for example in F_{B1-A1} or F_{B2-A2}. However, the terms $\alpha_1 i_1$ and $\alpha_2 i_2$ describe the influence of the coils and resistors on the motion of the magnets. A description of these terms and an analysis of energy recovery from magnet motion are presented in the next section. In this section, only the mechanical aspects and magnetic effects were presented.

2.1. Modeling of magnetic forces

The appropriate orientation of the magnets: SN–NS–SN–NS creates magnetic springs (see Fig. 1). The spring forces are symbolically described as F_{B1-A1}, F_{B2-A1}, F_{B1-A2}, F_{B2-A2} and F_{A2-A1}. The indexes indicate the magnets which generate respective magnetic forces. In this system, two pairs of identical magnets (A_1, A_2 and B_1, B_2) were applied. Therefore, the magnetic forces were experimentally determined for two cases. Characteristics of the interaction between one small and one large magnet (Case I) and between two larger magnets (Case II) were determined. In the tests, one of the magnets was stationary. The other movable magnet was loaded with an additional mass, and the change in the distance between both magnet centers (Δ_{A-A}or Δ_{B-A}) was measured. Curves obtained experimentally and their approximations using polynomials are presented in Fig. 2.

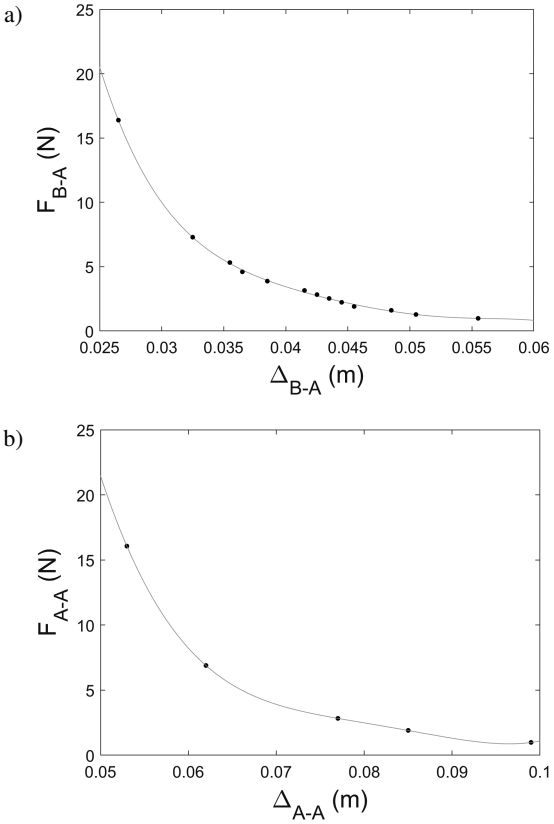

Fig. 2. Characteristics of magnetic suspensions: Case I a) and Case II b). Points – experimental data, solid line – polynomials fit

In both cases, the experimental data were fitted by 5$^{\text{th}}$ order polynomials:

$$F_{B-A} = a_0 + a_1\Delta_{B-A} + a_2\Delta_{B-A}^2 + a_3\Delta_{B-A}^3 + a_4\Delta_{B-A}^4 + a_5\Delta_{B-A}^5, \quad (3)$$

$$F_{A-A} = b_0 + b_1\Delta_{A-A} + b_2\Delta_{A-A}^2 + b_3\Delta_{A-A}^3 + b_4\Delta_{A-A}^4 + b_5\Delta_{A-A}^5 \quad (4)$$

with the obtained values of the polynomial coefficients being presented in Table 1.

In a subsequent step, forces F_{B1-A1}, F_{B2-A1}, F_{B1-A2}, F_{B2-A2} and F_{A2-A1} were related to the dependencies in equations (3), (4). This required writing distances Δ as a function of variables

Table 1
Values of polynomial coefficients, equations (3), (4)

Coefficient	Value	Coefficient	Value
a_0	534.588	b_0	668.828
a_1	–54878.708	b_1	–31972.138
a_2	2298250.857	b_2	578339.903
a_3	–48447629.279	b_3	–4659587.477
a_4	510470867.643	b_4	14056672.514
a_5	–2142177188.14	b_5	0

z_S, z_1 and z_2. The simplest way to do so was to determine F_{A2-A1} from equation (4), because the distance between the movable magnets was $\Delta_{A2-A1} = z_2 - z_1$. Hence, this force can be written in the following form:

$$\begin{aligned} F_{A2-A1} = {} & b_0 + b_1 (z_2 - z_1) \\ & + b_2 (z_2 - z_1)^2 + b_3 (z_2 - z_1)^3 \\ & + b_4 (z_2 - z_1)^4 + b_5 (z_2 - z_1)^5 . \end{aligned} \tag{5}$$

When analyzing the interaction between the movable magnet A_1 and the lower (F_{B1-A1}) or upper (F_{B2-A1}) fixed magnet, it can be assumed that the distance Δ_{B2-A1} should be larger than the horizontal axis range presented in Fig. 2a. Generally, the minimum distance Δ_{B2-A1} will be greater than 0.055 m, because at this value the magnets A_1, A_2 and B_2 would be in contact. This is a physical limit due to magnet length, as one and a half lengths of the large magnet plus half a length of the small magnet yields exactly 0.055 m. Consequently, force F_{B2-A1} for $\Delta_{B2-A1} > 0.055$ m is negligible. This term has been omitted in the model:

$$F_{B2-A1} = 0. \tag{6}$$

Interaction with a closer magnet F_{B1-A1} corresponds to the presented curve (Fig. 2a). However, the distance between the magnets is $\Delta_{B1-A1} = z_1 - z_s$, and the magnetic force can be calculated from:

$$\begin{aligned} F_{B1-A1} = {} & a_0 + a_1 (z_1 - z_S) \\ & + a_2 (z_1 - z_S)^2 + a_3 (z_1 - z_S)^3 \\ & + a_4 (z_1 - z_S)^4 + a_5 (z_1 - z_S)^5 . \end{aligned} \tag{7}$$

Repeating the same analysis for the second movable magnet (A_2) and the fixed magnets, the magnetic forces take the following forms:

$$F_{B1-A2} = 0, \tag{8}$$

$$\begin{aligned} F_{B2-A2} = {} & a_0 + a_1 (L + z_S - z_2) \\ & + a_2 (L + z_S - z_2)^2 + a_3 (L + z_S - z_2)^3 \\ & + a_4 (L + z_S - z_2)^4 + a_5 (L + z_S - z_2)^5 , \end{aligned} \tag{9}$$

where the distance between the upper fixed magnet and magnet A_2 is $\Delta_{B2-A2} = L + z_S - z_2$. The parameter L specifies the distance between the centers of the fixed magnets. In the tested system, the L value is 0.15 m. The experimental data and their analysis allowed us to determine magnetic forces.

Based on equations (1)–(9), the differential equations of motion, including only magnetic and gravity forces, can be written as:

$$\begin{aligned} & m_1 \ddot{z}_1 + m_1 g - \{ a_0 + a_1 (z_1 - z_S) \\ & \quad + a_2 (z_1 - z_S)^2 + a_3 (z_1 - z_S)^3 + a_4 (z_1 - z_S)^4 \\ & \quad + a_5 (z_1 - z_S)^5 \} + \{ b_0 + b_1 (z_2 - z_1) \\ & \quad + b_2 (z_2 - z_1)^2 + b_3 (z_2 - z_1)^3 + b_4 (z_2 - z_1)^4 \\ & \quad + b_5 (z_2 - z_1)^5 \} = 0, \end{aligned} \tag{10}$$

$$\begin{aligned} & m_2 \ddot{z}_2 + m_2 g + \{ a_0 + a_1 (L + z_S - z_2) \\ & \quad + a_2 (L + z_S - z_2)^2 + a_3 (L + z_S - z_2)^3 \\ & \quad + a_4 (L + z_S - z_2)^4 + a_5 (L + z_S - z_2)^5 \} \\ & \quad - \{ b_0 + b_1 (z_2 - z_1) + b_2 (z_2 - z_1)^2 \\ & \quad + b_3 (z_2 - z_1)^3 + b_4 (z_2 - z_1)^4 \\ & \quad + b_5 (z_2 - z_1)^5 \} = 0. \end{aligned} \tag{11}$$

Equations (10) and (11) enable the determination of movable magnet equilibrium positions. For a static case, accelerations ($\ddot{z}_1$, $\ddot{z}_2$) and kinematic excitation (z_S) are equal to 0. After solving equations (10), (11) for the above assumption, the values of variables z_1 and z_2 can be calculated. To distinguish these values, the defining equilibrium positions are marked as z_{1e} and z_{2e}. For different distances L between the fixed magnets, the obtained equilibriums are different, too. Knowing the equilibrium positions, natural frequencies for low vibrations can be determined. For this purpose, nonlinear curves from Fig. 2 should be linearized near the equilibrium position. Linearized relationships between the magnetic forces can be written as:

$$F_{B1-A1} = k_1 (z_1 - z_s) = k_1 (z_{1e} + z_{1d} - z_s) , \tag{12}$$

$$F_{A2-A1} = k_2 (z_2 - z_1) = k_2 (z_{2e} + z_{2d} - z_{1e} - z_{1d}) , \tag{13}$$

$$F_{B2-A2} = k_3 (L + z_S - z_2) = k_3 (L + z_S - z_{2e} - z_{2d}) , \tag{14}$$

where variables z_1 and z_2 respectively, consist of two parts: constant z_{1e} or z_{2e} (equilibrium position) and dynamic z_{1d} or z_{2d} (low vibration about the equilibrium position). Functions (12)–(14) describe the lines tangent to the nonlinear curves of magnetic force at equilibrium position points. Therefore, via linearization, linear stiffness coefficients are determined:

$$k_1 = \left. \frac{\mathrm{d}F_{B1-A1}}{\mathrm{d}\Delta_{B1-A1}} \right|_{\Delta_{B1-A1} = z_{1e} - z_s} , \tag{15}$$

$$k_2 = \left. \frac{\mathrm{d}F_{A1-A2}}{\mathrm{d}\Delta_{A1-A2}} \right|_{\Delta_{A1-A2} = z_{2e} - z_{1e}} , \tag{16}$$

$$k_3 = \left. \frac{\mathrm{d}F_{B2-A2}}{\mathrm{d}\Delta_{B2-A2}} \right|_{\Delta_{B2-A2} = L + z_s - z_{2e}} . \tag{17}$$

Substituting equations (12)–(14) into (1), (2), a linearized model without damping forces is obtained:

$$m_1\ddot{z}_{1d} + m_1 g - k_1(z_{1e} + z_{1d} - zs) + k_2(z_{2e} + z_{2d} - z_{1e} - z_{1d}) = 0, \tag{18}$$

$$m_2\ddot{z}_{2d} + m_2 g + k_3(L + z_S - z_{2e} - z_{2d}) - k_2(z_{2e} + z_{2d} - z_{1e} - z_{1d}) = 0. \tag{19}$$

Equations (18), (19) for a static case ($\ddot{z}_1 = \ddot{z}_2 = z_S = 0$) have the following form:

$$m_1 g - k_1(z_{1e}) + k_2(z_{2e} - z_{1e}) = 0, \tag{20}$$

$$m_2 g - k_3(z_{2e}) - k_2(z_{2e} - z_{1e}) = 0. \tag{21}$$

A comparison of equations (18), (19) with (20), (21) can simplify mathematical notation of the linearized model for natural vibrations ($z_s = 0$):

$$m_1\ddot{z}_{1d} - (k_1 + k_2)z_{1d} + k_2 z_{2d} = 0, \tag{22}$$

$$m_2\ddot{z}_{2d} - (k_3 + k_2)z_{2d} + k_2 z_{1d} = 0. \tag{23}$$

In equations (22), (23), the employed sign convention requires a comment because in the classical 2 DOF linear oscillator it is the reverse. This is due to the fact that, in linearization, the coefficients calculated from equations (15)–(17) will have negative values. Finally, after substituting the parameter value, the sign convention will follow the classical form of the linear model with the positive stiffness coefficients. By solving an eigenvalue problem for equations (22), (23), it is possible to calculate linear natural frequencies. Figure 3 presents the equilibrium positions and linear natural frequencies versus the distance L between the fixed magnets.

The curves in Fig. 3 show clear trends. When the distance L is increased, the coordinates of both equilibrium positions are higher. However, the trend with respect to changes in linear natural frequencies is the opposite. For a larger L, lower frequency values are obtained. The next step of the modeling was performed for L equal to 150 mm.

2.2. Identification of damping forces

In differential equations (1), (2), there still exist unknown damping forces F_{d1} and F_{d2}. In this system, the energy dissipation process is complex. It is assumed that the most important factors affecting the damping forces are air resistance and dry friction:

$$F_{d_1} = c_1\dot{z}_1 + c_2\dot{z}_1|\dot{z}_1| + T_1, \tag{24}$$

$$F_{d_2} = c_1\dot{z}_2 + c_2\dot{z}_2|\dot{z}_2| + T_2, \tag{25}$$

where c_1 and c_2 are the linear and nonlinear coefficients describing air resistance, and T_1 and T_2 are friction forces between the magnets and the tube.

The magnets are placed inside the tube to constrain free airflow. To reduce air resistance, special holes are made in the tube. The model of air resistance is nonlinear and it is the sum of linear and quadratic terms [20]. These terms are assumed to depend on the absolute velocities, and the damping coefficients are the same for both movable magnets (c_1, c_2). The final terms T_1 and T_2 denote the Coulomb friction. Magnetic interaction induces forces as well as a magnetic moment. This moment makes the movable magnet rotate in the tube. As a result, a two-point contact between the magnet and the tube is observed. This moment affects the normal forces at these points and, finally, the dry friction level. Proportional dependencies between normal and magnetic forces are assumed. Finally, dry friction takes the forms below:

$$\begin{aligned} T_1 &= \mu_0 N_1 \operatorname{sgn}(\dot{z}_1 - \dot{z}_S) \\ &= \mu_0(\varepsilon F_{B1-A1} + \varepsilon F_{A2-A1})\operatorname{sgn}(\dot{z}_1 - \dot{z}_S) \\ &= \mu(F_{B1-A1} + F_{A2-A1})\operatorname{sgn}(\dot{z}_1 - \dot{z}_S), \end{aligned} \tag{26}$$

$$\begin{aligned} T_2 &= \mu_0 N_2 \operatorname{sgn}(\dot{z}_2 - \dot{z}_S) \\ &= \mu_0(\varepsilon F_{B2-A2} + \varepsilon F_{A2-A1})\operatorname{sgn}(\dot{z}_2 - \dot{z}_S) \\ &= \mu(F_{B2-A2} + F_{A2-A1})\operatorname{sgn}(\dot{z}_2 - \dot{z}_S), \end{aligned} \tag{27}$$

where coefficient μ includes the friction coefficient μ_o and the scale factor between the magnetic and normal forces ε. A direct determination of the unknown coefficients of air resistance

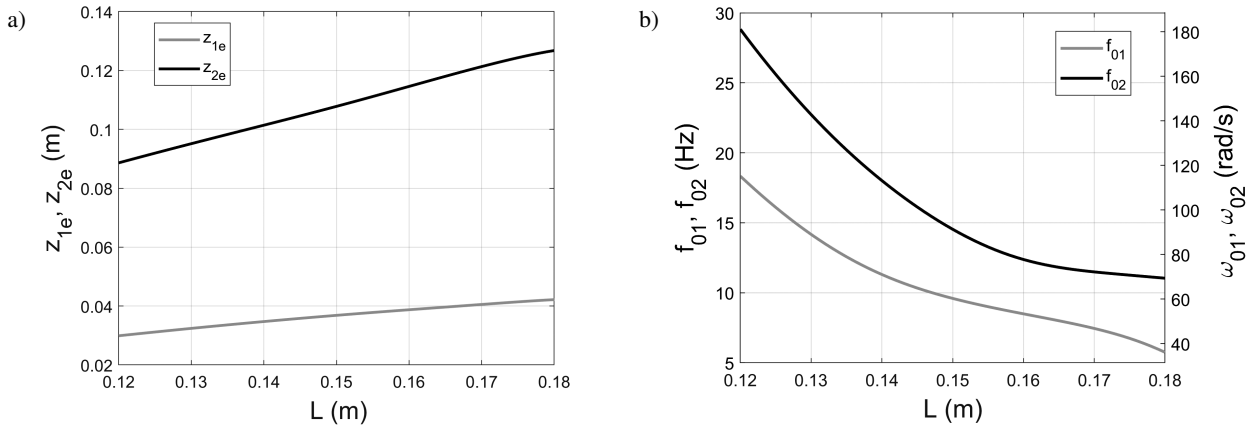

Fig. 3. Changes in equilibrium positions (a) and linear natural frequencies ($\omega_0 = 2\pi f_0$) (b) versus distance L

(c_1, c_2) and dry friction (μ) is difficult. Therefore, the damping parameters are estimated by comparing experimental and numerical dynamic responses.

Experiments are performed using the experimental setup presented in Fig. 4. The tested system with levitating magnets is mounted onto an electrodynamic shaker armature. Kinematic excitation is controlled by the LMS controller, which uses a signal from the accelerometer in a feedback loop. Magnet motion is measured in a contactless manner using the Phantom V9.1 high-speed camera.

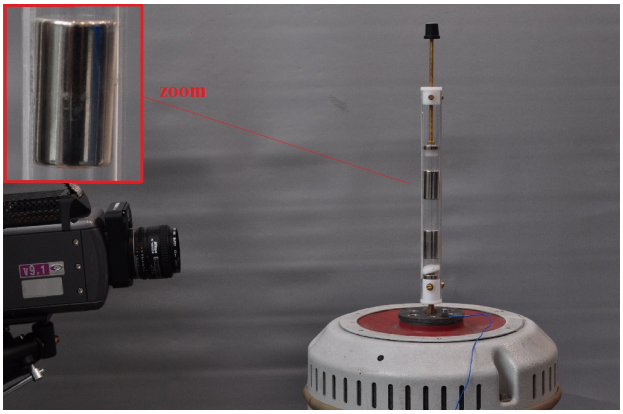

Fig. 4. View of the experimental setup

In the experiments, the coils and resistors were not added to the system because the application of an electrical system induces additional forces, which would prevent correct identification of the searched parameters. A sine test was performed on an electrodynamic shaker. Kinematic excitation with the constant acceleration amplitude of 0.6g was generated. However, the excitation frequency was swept linearly from 6 to 15 Hz. System responses were measured with a high speed camera. The excitation frequency was changed slowly, and the time of one test was set, equal to 180 s. Clips were recorded with a speed of 250 frames per second. An analysis of the visual data made it possible to determine absolute displacements z_S, z_1 and z_2 (Fig. 5).

Based on equations (1)–(9) and (24)–(27), the final form of the differential equations of motion can be written as:

$$\begin{aligned} &m_1\ddot{z}_1 + c_1\dot{z}_1 + c_2\dot{z}_1\left|\dot{z}_1\right| + m_1 g + \alpha_1 i_1 + \{a_0 \\ &\quad + a_1(z_1 - z_S) + a_2(z_1 - z_S)^2 + a_3(z_1 - z_S)^3 \\ &\quad + a_4(z_1 - z_S)^4 + a_5(z_1 - z_S)^5\}(-1 \\ &\quad + \mu\,\mathrm{sgn}(\dot{z}_1 - \dot{z}_S)) + \{b_0 + b_1(z_2 - z_1) \\ &\quad + b_2(z_2 - z_1)^2 + b_3(z_2 - z_1)^3 + b_4(z_2 - z_1)^4 \\ &\quad + b_5(z_2 - z_1)^5\}(1 + \mu\,\mathrm{sgn}(\dot{z}_1 - \dot{z}_S)) = 0, \end{aligned} \tag{28}$$

$$\begin{aligned} &m_2\ddot{z}_2 + c_1\dot{z}_2 + c_2\dot{z}_2\left|\dot{z}_2\right| + m_2 g + \alpha_2 i_2 \\ &\quad + \{a_0 + a_1(L + z_S - z_2) + a_2(L + z_S - z_2)^2 \\ &\quad + a_3(L + z_S - z_2)^3 + a_4(L + z_S - z_2)^4 \\ &\quad + a_5(L + z_S - z_2)^5\}(1 + \mu\,\mathrm{sgn}(\dot{z}_2 - \dot{z}_S)) \\ &\quad + \{b_0 + b_1(z_2 - z_1) + b_2(z_2 - z_1)^2 + b_3(z_2 - z_1)^3 \\ &\quad + b_4(z_2 - z_1)^4 + b_5(z_2 - z_1)^5\}(-1 \\ &\quad + \mu\,\mathrm{sgn}(\dot{z}_2 - \dot{z}_S)) = 0. \end{aligned} \tag{29}$$

The numerical model of the system, i.e. equations (28), (29), was developed using the Matlab software. Many simulations were performed for different values of parameters c_1, c_2 and μ. The values of other parameters are listed above. Only α_1 and α_2 are equal to zero, because at this stage of the analysis the system is without coils and resistors. The n points are obtained from each simulation. The number n corresponds to the number of captured images, i.e. $n = 180 \times 250 = 45000$. However, the time interval between the points depends on the camera recording speed $\Delta t = 1/250 = 0.004$ s. All i points from the obtained time series (z_{1i} or z_{2i} with the index num) are compared with the reference signals, experimental data (z_{1i} or z_{2i} with the index exp). The optimal values of these parameters are determined based on the minimization of objective function δ criterion:

$$\begin{aligned} &\min \delta(c_1, c_2, \mu) \\ &\quad \delta(c_1, c_2, \mu) = \max\{\delta_1(c_1, c_2, \mu),\ \delta_2(c_1, c_2, \mu)\}, \end{aligned} \tag{30}$$

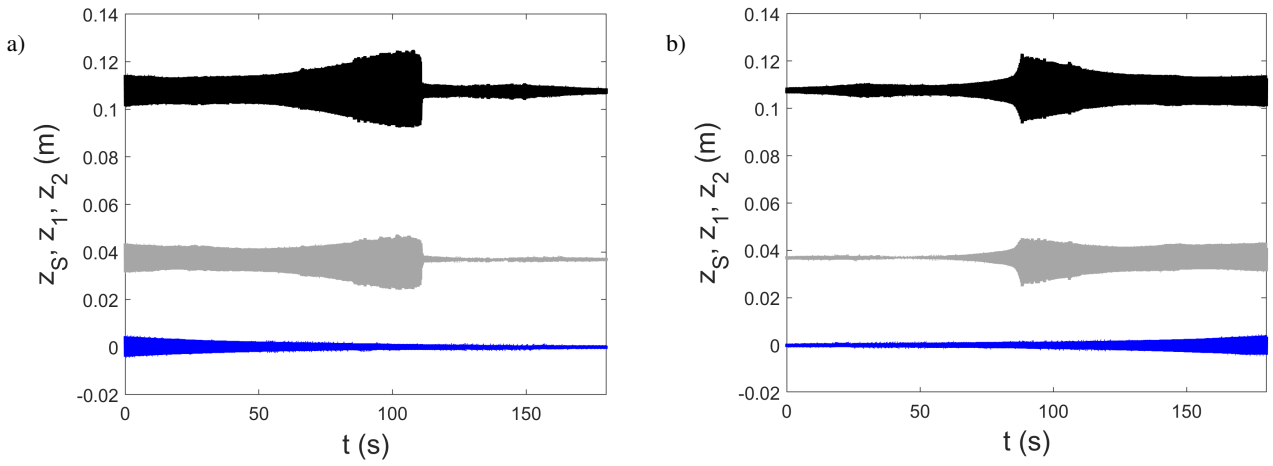

Fig. 5. Time series from the sine tests on the shaker: a) frequency forward, b) frequency backward. Blue line – z_S, gray line – z_1, black line – z_2

where the following relative errors are used:

$$\delta_1(c_1, c_2, \mu) = \sum_{i=1}^{n=45000} \left(z_{1,\text{num}} - z_{1,\text{exp}}\right)^2, \tag{31}$$

$$\delta_2(c_1, c_2, \mu) = \sum_{i=1}^{n=45000} \left(z_{2,\text{num}} - z_{2,\text{exp}}\right)^2. \tag{32}$$

The values of parameters c_1, c_2 and μ for simulations were randomly taken from the intervals: $(c_{1,\min};\ c_{1,\max})$, $(c_{2,\min};\ c_{2,\max})$, $(\mu_{\min};\ \mu_{\max})$. The minimum value was equal to 0. The maxima of the parameter domains were taken such that a single non-zero limit (for example $c_{1,\max}$ when $c_{2,\max} = \mu_{\max} = 0$) would give a negligibly small oscillation of the magnets. Performing more simulations makes it possible to find the optimal solution when equation (30) has the minimum value. Finally, the following damping model coefficients from the applied procedure were estimated: $c_1 = 0.0386$ Nsm^{-1}, $c_2 = 0067$ Ns^{2}m^{-2}, $\mu = 0.0347$ $(-)$.

Figure 6 shows a comparison of the time series obtained from the optimal simulation variant and experimental data. Both responses are similar. It should be emphasized that this is possible only when the normal force depends on the repulsive forces of the magnets. At the initial stage of this study, numerical simulations for the classical approach with constant normal forces were also performed. For this case, it was not possible to find responses similar to the experimental data.

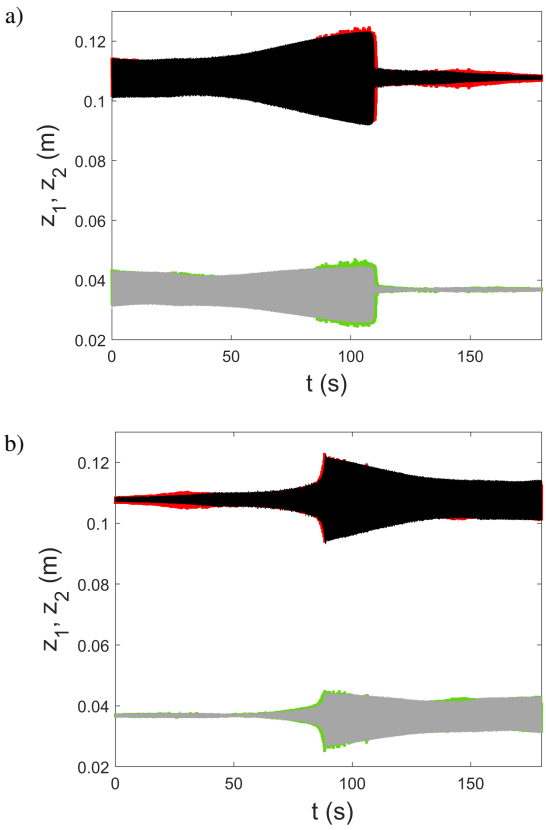

Fig. 6. Comparison of the time series from optimal simulation and experimental data: a) frequency forward, b) frequency backward. Gray line – $z_{1,\text{num}}$, black line – $z_{2,\text{num}}$, red line – $z_{1,\text{exp}}$, green line – $z_{2,\text{exp}}$

The obtained responses confirm the existence of a hardening effect. It is more visible for the resonance characteristics obtained from the numerical results (Fig. 7). For the forward frequency sweep (solid line), the amplitude jump is visible for a higher excitation frequency of about 11.4 Hz. For the backward frequency sweep (dashed line), the amplitude jump is observed for a lower frequency of about 10.7 Hz.

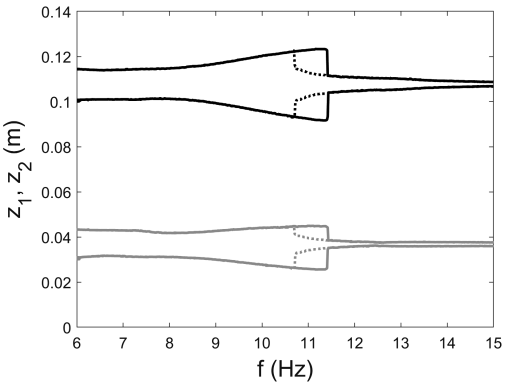

Fig. 7. Characteristics of maximum and minimum values of system responses. Simulations made with the constant excitation acceleration amplitude of 0.6g. Solid line – forward frequency, dashed line – backward frequency, gray line – z_1, black line – z_2

The tested system has two degrees of freedom, so two resonance regions can be expected. The time series clearly show the existence of one such region. To identify the second resonance region, higher excitation is required, for example 1.5g for the excitation frequencies near the second resonance zone. However, the excitation amplitude of 0.7g gives oscillations near the physical limit in the first resonance zone. The magnet distance Δ_{A2-B2} must be larger than the sum of half a length of the smaller magnet and half a length of the larger magnet. Hence, relative motion $x_2 - x_S$ should be smaller than 0.13 m (L minus the above sum). For the application of a slightly higher excitation level, this limit is not satisfied, and impacts of the magnets are generated. On the other hand, the existence of friction constrains motion when the shaker amplitude was reduced. Cases when dry friction is a barrier to the magnet relative motion were also observed. Due to significant friction, for this system it is not possible to experimentally find resonance regions for low vibrations and to directly compare them with the results of the linearized model (Fig. 3b). The visible resonance area in the resonance curves (Fig. 7) is shifted towards higher frequencies by the hardening effect. This system is specific because the magnet's motion without impact and stopping is possible for a very narrow level of excitation.

Therefore, in this study, system vibrations with a 0.6g excitation amplitude are investigated.

3. ANALYSIS OF ENERGY RECOVERY

In this section, we examine the developed model. Equations (28), (29) have been supplemented with electrical components (coils and resistors). The analysis of harvester properties is theoretical. For the time being, inductive coils have not been made.

Results obtained give some guidelines for their design. Generally, mathematical description is based on previous studies of a system with one degree of freedom [12–14]. The electrical equations of electrical circuits can be written in the following forms:

$$L_{C1}\ddot{q}_1 + R_1\dot{q}_1 = \alpha_1\left(\dot{z}_1 - \dot{z}_S\right), \tag{33}$$

$$L_{C2}\ddot{q}_2 + R_2\dot{q}_2 = \alpha_2\left(\dot{z}_2 - \dot{z}_S\right), \tag{34}$$

where L_{C1} and L_{C2} are the inductances of both inductance coils, while R_1 and R_2 stand for total resistance in the first and second electrical circuits. Total resistance is the sum of the resistance of the coil and resistor in its circuit. Electric variables are charges q_1 and q_2, whereas α_1 and α_2 are the electromechanical coupling coefficients. Equations (33), (34) are independent. Therefore, it is assumed that the upper magnet motion does not generate current in the bottom coil and vice versa. This is possible when the distance between the coils, coil length and magnet vibration level are properly selected. An example of a configuration with one magnet and two coils is presented in Fig. 8. Nonlinear curves of the electromechanical coupling coefficient are visible. The curves reach the minimum and maximum values when the magnet center coincides with one end of the coil. In the presented case, the magnet in equilibrium position has the maximum electromechanical coupling coefficient. Now, if the magnet vibrations are appropriately smaller than the distance between the coils, the magnet will generate current only in the closer coil. The electromotive forces in the coils will depend on the curve region: a red curve region around the maximum value and a blue curve region where the values are close to zero. The second simplification relates to the constant value of the coupling coefficient. In the literature one can find studies in which an equivalent constant value is used [16]. It can also be explained by Fig. 8. If only a portion of the red curve near its maximum is used, then this shape can be described as the sum of the constant and some nonlinear terms. In the first order of approximation, only a constant value of the electromechanical coupling coefficient can be applied.

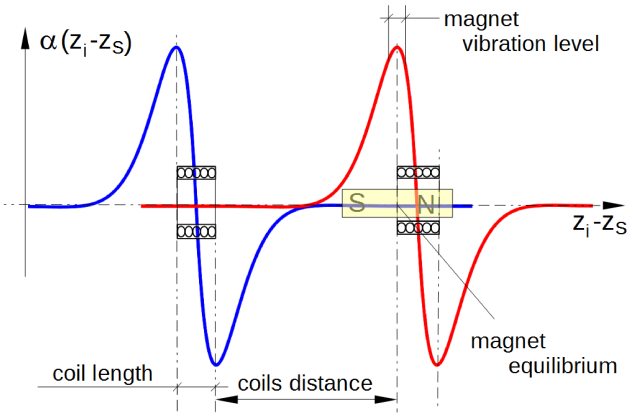

Fig. 8. Examples of curves of electromechanical coupling coefficient versus magnet position in relation to the coils. The coupling between magnet and right coil (red), the coupling between magnet and left coil (blue)

Generally, inductances L_{C1} and L_{C2} are much lower than total resistances R_1 and R_2. Consequently, the inductances can be omitted and the equations can be written as:

$$i_1 = \dot{q}_1 = \frac{\alpha_1}{R_1}\left(\dot{z}_1 - \dot{z}_S\right), \tag{35}$$

$$i_2 = \dot{q}_2 = \frac{\alpha_2}{R_2}\left(\dot{z}_2 - \dot{z}_S\right), \tag{36}$$

where i_1 and i_2 are the currents. Equations (28), (29) contain electrical terms $\alpha_1 i_1$ and $\alpha_2 i_2$. Substituting equations (35), (36), we obtain:

$$\alpha_1 i_1 = \frac{\alpha_1^2}{R_1}\left(\dot{z}_1 - \dot{z}_S\right) = c_{1e}\left(\dot{z}_1 - \dot{z}_S\right), \tag{37}$$

$$\alpha_2 i_2 = \frac{\alpha_2^2}{R_2}\left(\dot{z}_2 - \dot{z}_S\right) = c_{2e}\left(\dot{z}_2 - \dot{z}_S\right). \tag{38}$$

Substituted with the new forms of the electrical terms, equations (37), (38) show that the system has additional damping, the so-called electrical damping. Their coefficients c_{1e} and c_{2e} depend on the values of total resistance and electromechanical coupling coefficients. In this study, it was assumed that the coupling coefficients α_1 and α_2 are constant and equal to 20 Vsm^{-1}. The proposed value has a level similar to that from our previous studies with the single magnet [13, 14]. However, the values of the coefficients have been reduced, because after adding the second coil the total electrical damping in the system should not be too excessive. The power of recovered energy can be written as follows:

$$P_1 = R_1 i_1^2 = \frac{\alpha_1^2}{R_1}\left(\dot{z}_1 - \dot{z}_S\right)^2, \tag{39}$$

$$P_2 = R_2 i_2^2 = \frac{\alpha_2^2}{R_2}\left(\dot{z}_2 - \dot{z}_S\right)^2. \tag{40}$$

Numerical simulations were made for equations (28), (29), considering the new notation of electrical terms, i.e. equations (37), (38).

3.1. Primary case analysis

The so-called primary case was a system with a spacing between the magnets $B_1 - B_2$ made equal to $L = 150$ mm. This case was chosen as primary because the experimental dynamics tests to identify damping forces were performed for it. A numerical analysis was continued for this fixed magnet distance, where the values of resistances were predominantly varied. However, the considerations were limited to the variants where the resistances of both harvesters were the same, i.e. $R_1 = R_2$. Test results obtained for the system with connected energy recovery circuits are shown in Fig. 9 and 10.

A certain part of mechanical energy is converted into electrical energy, but electrical damping affects the system oscillations. A lower resistance generates higher electrical damping (see equations (37), (38)). Therefore, in Fig. 9a we can see a significant reduction in the hardening effect ($R_1 = R_2 = 2$ kΩ). For a higher resistance of 10 kΩ, hardening reduction is small.

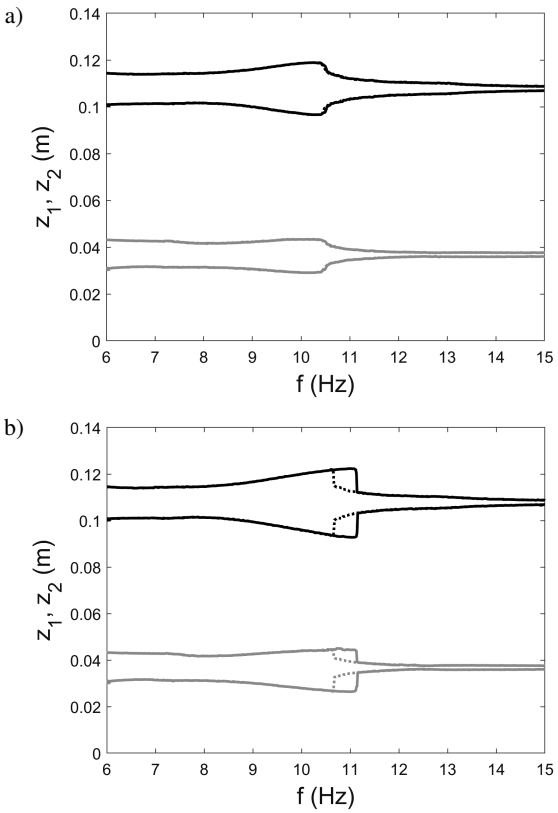

Fig. 9. Characteristics of maximum and minimum values of system responses. Simulations were made with the constant excitation acceleration amplitude of 0.6g and resistances a) $R_1 = R_2 = 2000\ \Omega$ and b) $R_1 = R_2 = 10000\ \Omega$. Solid line – forward frequency, dashed line – backward frequency, gray line – z_1, black line – z_2

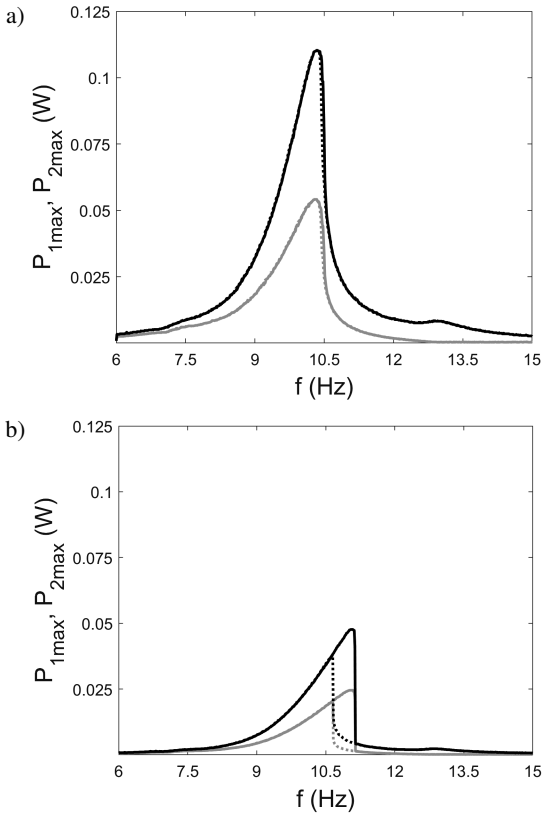

Fig. 10. Characteristics of maximum values of power recovery energy. Simulations were made with the constant excitation acceleration amplitude of 0.6g and resistances a) $R_1 = R_2 = 2000\ \Omega$ and b) $R_1 = R_2 = 10000\ \Omega$. Solid line – forward frequency, dashed line – backward frequency, gray line – P_1, black line – P_2

Equations (39), (40) are quadratic terms. Therefore, the energy power can change from 0 to the maximum value. Figure 10 provides two important pieces of information. First, in both resistance cases the power recovery is lower for the bottom movable magnet (gray line) than for the upper movable magnet (black line). The greater power recovery P_2 is approximately two times higher than the second value P_1. The ratio $P_2 : P_1$ in the peaks is 0.1103 W:0.05413 W= 2.0377 (Fig. 10a) and 0.04765 W:0.02453 W= 1.9425 (Fig. 10b). This trend results from the fact that upper magnet oscillations are larger than those of the bottom movable magnet (Fig. 9). Probably the gravity forces of movable magnets shift their equilibriums closer to the lower fixed magnet and this may predispose the upper movable magnet to larger vibrations. Secondly, equations (39), (40) suggest that for increasing power, resistance should be as low as possible and the vibration relative speed should be as high as possible. However, energy recovery is higher for the curves in Fig. 10a when both factors are lower. In this case, the resistances have smaller values ($R_1 = R_2 = 2000\ \Omega < 10000\ \Omega$). In contrast, the amplitudes in Fig. 9a are smaller than those in Fig. 9b. Therefore, it can be supposed that the vibration velocities will also be lower when the resistances are equal to 2000 Ω. Performed additional calculations confirmed that relative magnet velocities were larger for $R_1 = R_2 = 10000\ \Omega$. These maximum amplitudes of relative velocities for top and bottom magnets were 0.773 m/s and 0.469 m/s or 1.11 m/s and 0.74 m/s, respectively, for resistance 2 kΩ and 10 kΩ. Figures 9 and 10 show the characteristics only for two selected cases. The curves show that resistance affects magnet vibration and energy recovery. For maximum energy recovery, the optimal resistance will probably be a compromise between magnet vibration and energy recovery. To find the optimal resistance value, more curves were plotted. Obtained results are presented as color maps (Figs. 11 and 12).

More curves allow for a better understanding of the influence of resistance on magnet dynamics and energy recovery. For simplicity's sake, it can be generalized that reduction in resistance values leads to lower magnet vibrations and greater energy recovery. Therefore, some mechanical energy is transformed into electricity. On each map, the global maximum is shown as a white point. These points in Fig. 11 mark the high resistance when electrical damping is lower (see equations (37), (38)). Large vibrations do not guarantee the greatest energy recovery. The maximum level of electrical powers results from a compromise between vibration velocity and resistance value (see equations (39), (40)). Optimal resistance for the upper and bottom harvester can be determined from the location of a white point in Fig. 12. Generally, both harvesters have different locations of the optimal solution. The upper harvester produces the

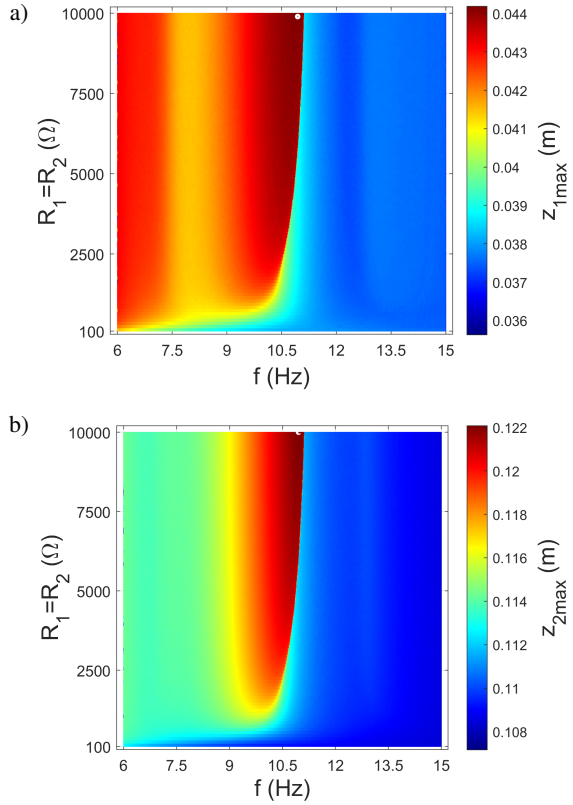

Fig. 11. Color maps showing the maximum z_1 (a) and maximum z_2 (b) versus resistance and excitation frequency. The maps were obtained with forward frequency sweep and 0.6g excitation amplitude. The white point marks the global maximum

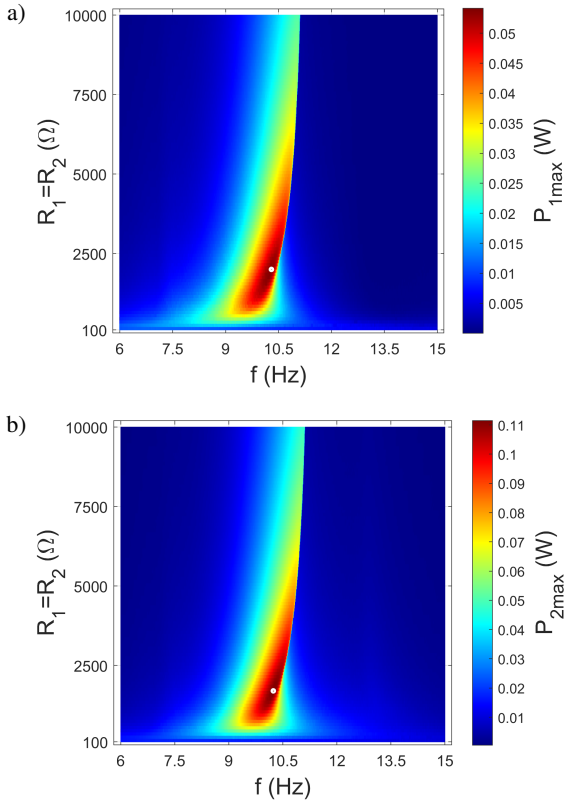

Fig. 12. Color maps showing the maximum P_1 (a) and maximum P_2 (b) versus resistance and excitation frequency. The maps were obtained with forward frequency sweep and 0.6g excitation amplitude. The white point marks the global maximum

most energy when $R_1 = R_2 = 1981\ \Omega$. The bottom harvester generates the maximum power for $R_1 = R_2 = 1634\ \Omega$.

Optimal resistances are different for each harvester. Therefore, a simple collective criterion has been applied. Recovery energy is dissipated on the resistors in a heat form, which depends on electrical power. Heating efficiency can be defined as the sum of the heats generated in both resistors. Analogically, the process is optimal when the sum of P_1 and P_2 reaches the maximum value. In the next section, maps of the collective criterion are shown. For the case under analysis, the location of the optimal point is visible in Fig. 13d. It is $R_1 = R_2 = 1634\ \Omega$, when the obtained sum of the maximum electric powers is equal to 0.1652 W. This optimal case occurs for an excitation frequency of 10.21 Hz. This value is close to the first linear natural frequency (see Fig. 3).

Summing up, the results show the possibility of energy recovery at a low level. For example, Fig. 10 shows that the maximum electrical power for the selected resistance values ($R_1 = R_2 = 2\ \text{k}\Omega$) is about 110.3 mW and 54.13 mW for the upper and bottom harvester, respectively. In the numerical analysis based on the sum of powers, the optimal resistance value was found to be $R_1 = R_2 = 1634\ \Omega$ (Fig. 13d). In this case, the recovered energy power changed insignificantly to 112 mW and 53.2 mW for the upper and bottom harvester, respectively. This shows that around the optimal point there exists a certain area where the energy recovery level is very similar.

3.2. Influence of distance *L*

The analysis of the so-called primary case ($L = 150$ mm) has been described above. In this section, the analysis was extended to cover other variants of distance L between the fixed magnets. Based on the numerical simulations, color maps have been created (Fig. 13). The main focus was on determining the influence of distance L on energy recovery. Therefore, the maps show the sum of the maximum powers from both harvesters versus load resistance and distance L.

Two aspects should be given particular attention when analyzing the color maps. They are: the white point location and the scale level of the color bar. This information describes the influence of distance L on optimal resistance and the maximum energy recovered. The maximum value of the color scale (see color bars in Fig. 13) increases with distance L. The maximum values correspond to the maximum sum of maximum powers P_1 and P_2. For the smallest distance $L = 135$ mm, the maximum sum is 14.18 mW (Fig. 13a). For a subsequent L, the level of recovered energy increases. Finally, for the highest tested value of $L = 170$ mm, the maximum sum is 491.6 mW (Fig. 13h). This trend can be clearly observed. If we want to recover more energy, we have to use a larger distance L between the fixed magnets. The influence of L on the optimal resistance value is not unequivocal. As distance L increases, the optimal resistances have the following values: 2476 Ω, 1832 Ω, 1783 Ω, 1634 Ω, 1486 Ω, 1783 Ω, 2426 Ω and 1832 Ω. To simplify, it can be as-

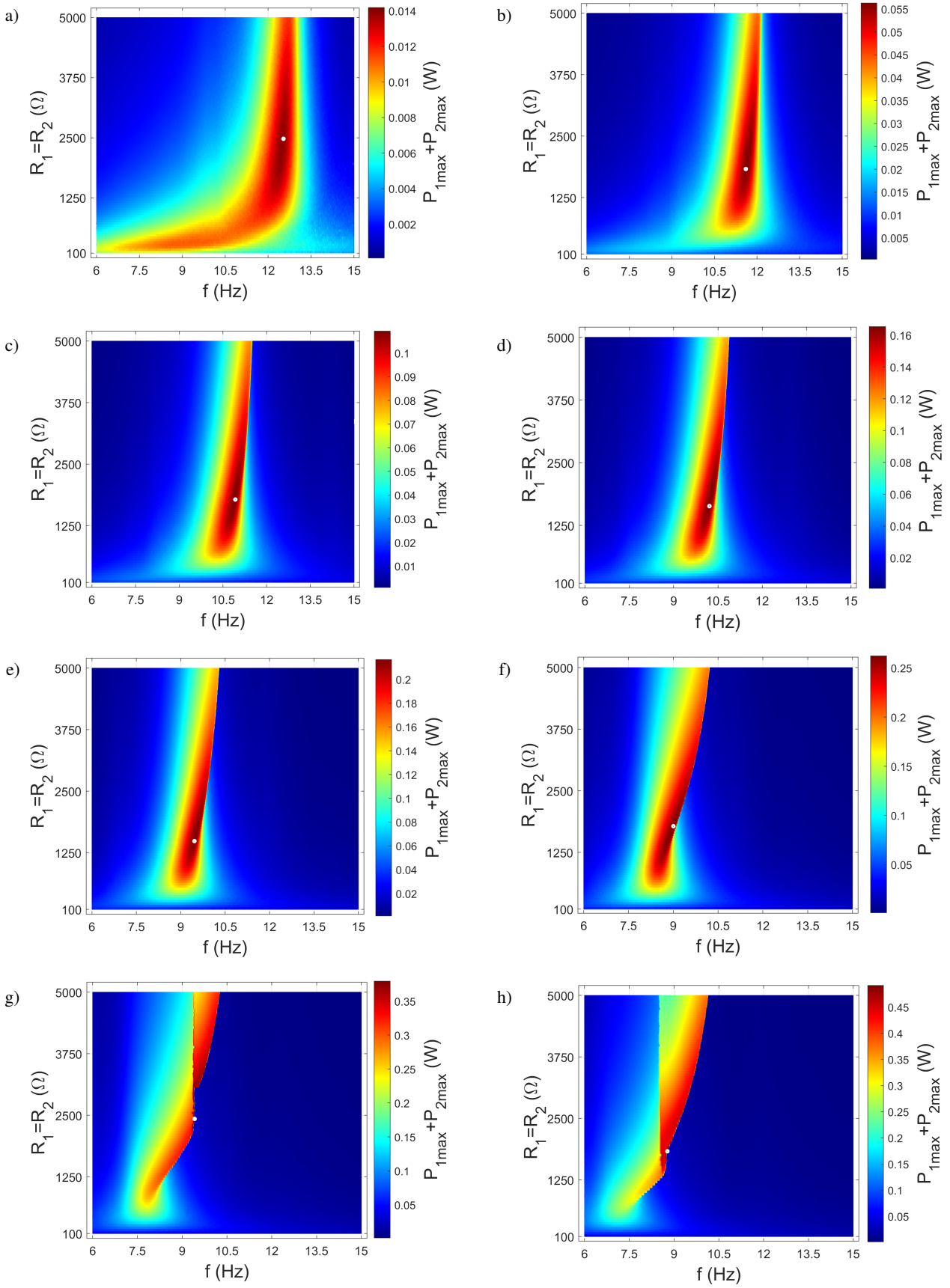

Fig. 13. Color maps showing the sum of maximum P_1 and maximum P_2 versus resistance and excitation frequency when L is equal to: 0.135 m (a), 0.14 m (b), 0.145 m (c), 0.15 m (d), 0.155 m (e), 0.16 m (f), 0.165 m (g), 0.17 m (h). The maps were obtained with forward frequency sweep and 0.6g excitation amplitude. The white point marks the global maximum

sumed that the optimal resistance for this system is about 2 kΩ. However, the maximum energy recovery can be closely related to the resonance phenomenon. Figure 3 shows that an increase in L leads to reduction in the natural frequencies. The optimal white point location on the maps changes in a similar manner. For $L = 135$ mm, the optimal point is observed when the excitation frequency is equal to 12.54 Hz. For a higher distance L, the optimal point shifts towards lower values. Finally, for $L = 170$ mm, the optimal point is located at 9.772 Hz.

4. CONCLUSIONS

This study focused on the modeling and analysis of an electromagnetic system with two levitation magnets. The conclusions can be grouped into two areas.

The first group of comments relates to the problem of friction. This issue is not widely considered in the literature, but this study has shown that it can be important in a system with two levitating magnets. The experimental data were approximated by the developed model only when the friction effect was considered. In addition, the normal forces had to be dependent on the magnetic forces. The problem will be analyzed in the future. The authors would like to verify the experimentally determined relationship between normal and magnetic forces. However, it is not an easy task in the proposed 2DOF system.

The other group of conclusions relate to the energy recovery process. The influence of resistance on the magnet dynamics and obtained electrical power was presented. As expected, with higher energy recovery the magnet vibrations decreased. For the assumed electromechanical coupling coefficient, optimal resistance was estimated. It was assumed to be about $R_1 = R_2 = 2$ kΩ. For different values of L optimal resistance could change by about 25%. These changes may result from the existence of non-linear mechanical damping, for example the friction effect. For a single harvester there exists a relationship between optimal resistance, the equivalent electromechanical coupling coefficient and the equivalent mechanical linear damping coefficient [16]. For different values of L, such equivalent mechanical linear damping coefficient would probably also be different. In the future, the use of other energy recovery system configurations will be considered, e.g. one coil between two movable magnets.

ACKNOWLEDGEMENTS

This work was financially supported under the project of the National Science Centre according to decision No. DEC-2019/35/B/ST8/01068.

REFERENCES

[1] Communication from the commission A Clean Planet for all, A European strategic long-term vision for a prosperous, modern, competitive and climate neutral economy. [Online] Available: https://eur-lex.europa.eu/legal-content/EN/TXT/?uri=CELEX:52018DC0773 [Accessed: 12 Nov. 2021].

[2] J. Kicinski, "Green energy transformation in Poland," *Bull. Pol. Acad. Sci. Tech. Sci.*, vol. 69, no. 1, p. e1362133(1–15), 2021, doi: 10.24425/bpasts.2020.136213.

[3] P.B. Abadi, D. Darlis, and M.S. Suraatmadja, "Green energy harvesting from human footsteps," *MATEC Web Conf.*, vol. 197, p. 11015(1–4), 2018, doi: 10.1051/matecconf/201819711015.

[4] G.D. Pasquale, A. Soma, and F. Fraccarollo, "Comparison between piezoelectric and magnetic strategies for wearable energy harvesting," *J. Phys.: Conf. Ser.*, vol. 476, p. 012097(1–5), 2013, doi: 10.1088/1742-6596/476/1/012097.

[5] C. Covani and A. Gontean, "Piezoelectric energy harvesting solutions: a review," *Sensors*, vol. 20: p. 3512(1–37), 2020, doi: 10.3390/s20123512.

[6] H. Elahi, M. Eugeni, and P. Gaudenzi, "A review on mechanisms for piezoeletric-based energy harvesters," *Energies*, vol. 11, p. 1850(1–35), 2018, doi: 10.3390/en11071850.

[7] M.R. Sarker, M.H. Saad, J.L. Olazagoitia, and J. Vinolas, "Review of power convert impact of electromagnetic energy harvesting circuits and devices for autonomous sensor applications," *Electronics*, vol. 10, p. 1108(1–35), 2021, doi: 10.3390/electronics10091108.

[8] L. Dal Bo and P. Gardonio, "Comparison between electromagnetic and piezoelectric seismic vibration energy harvesters," in *Proc. of International Conference on Noise and Vibration Engineering (ISMA 2016) and International Conference of Uncertainty in Structural Dynamics (USD 2016)*, 2016, pp. 681–694.

[9] M. Ostrowski, B. Blachowski, M. Bochenski, D. Piernikarski, P. Filipek, and W. Janicki, "Design of nonlinear electromagnetic energy harvester equipped with mechanical amplifier and spring bumpers," *Bull. Pol. Acad. Sci. Tech. Sci.*, vol. 68, pp. 1373–1383, 2020, doi: 10.24425/bpasts.2020.135384.

[10] J. Snamina and B. Sapinski, "Energy balance in self-powered MR damper – based vibration reduction system," *Bull. Pol. Acad. Sci. Tech. Sci.*, vol. 59, pp. 75–80, 2011, doi: 10.2478/v10175-011-0011-4.

[11] K. Kecik, A. Mitura, and J. Warminski, "Efficiency analysis of an autoparametric pendulum vibration absorber," *Eksploatacja i Niezawodność – Maintenance and Reliability*, vol. 15, pp. 221–224, 2013.

[12] K. Kecik and A. Mitura, "Energy recovery from a pendulum tuned mass damper with two independent harvesting sources," *Int. J. Mech. Sci.,* vol. 174, p. 105568(1–16), 2020, doi: 10.1016/j.ijmecsci.2020.105568.

[13] K. Kecik, A. Mitura, S. Lenci, and J. Warminski, "Energy harvesting from a magnetic levitation system," *Int. J. Non-Linear Mech.*, vol. 94, pp. 200–206, 2017, doi: 10.1016/j.ijnonlinmec.2017.03.021.

[14] K. Kecik, A. Mitura, J. Warminski, and S. Lenci, "Foldover effect and energy output from a nonlinear pseudo-maglev harvester," *AIP Conf. Proc.*, vol. 1922, p. 100009(1–7), 2018, doi: 10.1063/1.5019094.

[15] A.J. Sneller and B.P. Mann, "On the nonlinear electromechanical coupling between a coil and a oscillating magnet," *J. Phys. D: Appl. Phys.*, vol.43, p. 295005(1–10), 2010, doi: 10.1088/0022-3727/43/29/295005.

[16] M. Mosch and G. Fischerauer, "A comparison of methods to measure the coupling coefficient of electromechanical vibration energy harvesters," *Micromachines*, vol. 10, p. 0826(1–14), 2019, doi: 10.3390/mi10120826.

[17] I. Abed, N. Kacem, M.L Bouazizi, and N. Bouhaddi, "Nonlinear 2-dofs vibration energy harvester based on magnetic levitation," *Shock Vib. Aircr. Aerosp. Energy Harvesting*, vol. 9, pp. 39–45, 2015.

[18] P.L. Green, K. Worden, and N.D. Sims, "On the identification and modelling of friction in a randomly excited energy harvester," *J. Sound Vib.*, vol. 332, pp. 4696-4708, 2013, doi: 10.1016/j.jsv.2013.04.024.

[19] K. Kecik and A. Mitura, "Effect of variable friction on electromagnetic harvester dynamics," *Eur. Phys. J. Spec. Top.*, vol. 231, pp. 1433–1441, 2022, doi: 10.1140/epjs/s11734-022-00493-x.

[20] R. Salamon, H. Kaminski, and P. Fritzkowski, "Estimation of parameters of various damping models in planar motion of a pendulum", *Meccanica*, vol. 55, pp. 1655–1677, 2020, doi: 10.1007/s11012-020-01197-z.